ADVANCED FUNCTIONAL MATERIALS
www.afm-journal.de

Engineering of Multifunctional Nano-Micelles for Combined Photothermal and Photodynamic Therapy Under the Guidance of Multimodal Imaging

*Hua Gong, Ziliang Dong, Yumeng Liu, Shengnan Yin, Liang Cheng, Wenyao Xi, Jian Xiang, Kai Liu, Yonggang Li, and Zhuang Liu**

The integration of diagnostic and therapeutic functionalities on a single theranostic nano-system holds great promise to enhance the accuracy of diagnosis and improve the efficacy of therapy. Herein, a multifunctional polymeric nano-micelle system that contains a photosensitizer chlorin e6 (Ce6) is successfully fabricated, at the same time serving as a chelating agent for Gd^{3+}, together with a near-infrared (NIR) dye, IR825. With a r_1 relativity 7 times higher than that of the commercial agent Magnevist, strong fluorescence offered by Ce6, and high NIR absorbance attributed to IR825, these theranostic micelles can be utilized as a contrast agent for triple modal magnetic resonance (MR), fluorescence, and photoacoustic imaging of tumors in a mouse model. The combined photothermal and photodynamic therapy is then carried out, achieving a synergistic anti-tumor effect both in vitro and in vivo. Different from single photo treatment modalities which only affect the superficial region of the tumor under mild doses, the combination therapy at the same dose using this agent is able to induce significant damage to both superficial and deep parts of the tumor. Therefore, this work presents a polymer based theranostic platform with great potential in multimodal imaging and combination therapy of cancer.

1. Introduction

Phototherapy generally falls into two major categories, namely the photothermal therapy (PTT) and the photodynamic therapy (PDT), both of which are deemed as minimal invasive and effective approaches for cancer treatment.[1] PTT usually employs the photothermal agents that have strong absorbance in the near-infrared (NIR) region to generate heat, leading to thermal ablation of target cells.[2] While PDT relies on the photosensitizer to transfer photo energy to the surrounding oxygen molecules, generating reactive oxygen species, such as singlet oxygen (SO) to kill tumor cells.[3] Owing to the tumor targeting ability of appropriately design photosensitizers or photothermal agents, as well as the selective light irradiation of the lesion region, phototherapies exhibit remarkably reduced side effects and improved selectivity compared with traditional remedies.

In recent years, imaging guided therapy has been introduced as a new concept in cancer treatment, and shows promise in the optimization of therapeutic efficiency.[4–8] Imaging is particularly important for phototherapy.[9–15] Firstly, imaging could provide useful information such as size and location of the tumor, as well as the relationship of the tumor with surrounding tissues, helpful for determining the irradiation position, scope and optical dose. Secondly, imaging could provide the optimal time window for phototherapy so that the irradiation could be conducted when the phototherapeutic agent reaches the peaked level in the targeted lesion. Lastly, imaging is important to monitor the proceeding of diseases after therapy. It is thus important to design and engineer multifunctional theranostic agents that integrate imaging and therapy functionalities into a single nano-platform for imaging guided phototherapy.[16,17]

On the other side, owing to unsatisfactory results obtained from single therapeutic treatment, closer attentions have been paid to the development of combination therapy, which could dramatically enhance the therapeutic outcomes and minimize the side effects. Abundant combination choices, including "PTT + chemotherapy"[18–23], "PDT + chemotherapy"[24,25], as well as "PTT + PDT"[26–28], have been frequently adopted by researchers, aiming to achieve a synergistic effect in destructing cancer. To realize combined PDT and PTT, in particular, plenty of nanomaterials have been explored, including gold nanomaterials[29–31], graphene oxide (GO)[32,33], as well as upconversion nanoparticles (UCNPs)[34]. Despite the encouraging treatment

H. Gong, Z. L. Dong, Dr. L. Cheng, W. Y. Xi, J. Xiang, Dr. K. Liu, Prof. Z. Liu
Institute of Functional Nano & Soft Materials (FUNSOM)
Collaborative Innovation Center of Suzhou Nano Science and Technology
Soochow University
Suzhou, Jiangsu 215123, China
E-mail: zliu@suda.edu.cn
Y. M. Liu, S. Yin, Prof. Y. G. Li
Department of Radiology
the First Affiliated Hospital of Soochow University
Suzhou, Jiangsu 215006, China

DOI: 10.1002/adfm.201401451

© 2014 WILEY-VCH Verlag GmbH & Co. KGaA, Weinheim

results in various animal models as presented by those reports, most of the materials currently developed for combined PDT and PTT are inorganic-based ones, whose long term retention and potential toxicity are of great concerns. Therefore, the development of biocompatible organic agents with both photothermal and photodynamic functions, moreover, together with imaging abilities, may be of great importance to further push forward the future clinical use of imaging-guided combination phototherapy.

In our previous work, we have reported that a new type of NIR dye, IR825, an analog of indocyanine green (ICG), after being encapsulated into polyethylene glycol (PEG) coated nano-micelles could be used for effective tumor ablation.[35] In this work, we re-design our system and hope to realize imaging-guided combined photothermal and photodynamic therapy of cancer. Poly(maleic anhydride-alt-1-octadecene) (C18PMH) is firstly co-conjugated with a long PEG-amine (5 kDa) and a short biamine-PEG (324 Da), obtaining C18PMH-PEG_{5k}/PEG_{324}-NH_2 which is then conjugated with chlorin e6 (Ce6). The resulted Ce6 grafted amphiphilic polymer (abbreviated as C18PMH-PEG-Ce6) can be utilized to encapsulate IR825, resulting in IR825@C18PMH-PEG-Ce6 nano-micelles that contain both photosensitizer and photothermal agents. In addition, it is for the first time found that Ce6 as fluorophore and photosensitizer could also serve as a chelating agent to capture gadolinium-III, enabling T_1-contrast in magnetic resonance (MR) imaging. Notably, the r_1 relaxivity of IR825@C18PMH-PEG-Ce6-Gd appears to be ~ 7 times higher than that of Magnevist, a clinic approved T_1 weighted MR contrast agent. Utilizing the multi-functional IR825@C18PMH-PEG-Ce6-Gd nano-micelles, triple modal fluorescence, MR, and photoacoustic imaging-guided combined photothermal and photodynamic therapy is conducted with a mouse tumor model, achieving encouraging therapeutic outcomes with a noticeable synergistic anti-tumor effect.

2. Results and Discussion

2.1. Characterization of IR825@C18PMH-PEG-Ce6-Gd

The C18PMH-PEG_{5k}/$PEG_{324}NH_2$ polymer was synthesized according to the procedures described in the experimental section. Ce6 molecules were then conjugated to the amino groups in the C18PMH-PEG_{5k}/$PEG_{324}NH_2$ polymer through the amide bond. From the ^1H nuclear magnetic resonance (NMR) spectra of the obtained polymers at different synthetic steps (Supporting Information, Figure S1a–c), it was estimated that ≈43% of carboxyl groups on the C18PMH backbone were conjugated with mPEG$_{5k}$-NH_2, while ≈41% of carboxyl groups were conjugated with small molecular diamino PEG, onto 72% of which Ce6 molecules were anchored.

We next used the obtained C18PMH-PEG-Ce6 polymer to encapsulate IR825, which is a water-insoluble NIR-absorbing molecule synthesized based on our previously published protocol (**Scheme 1**).[35] The loading capacities of Ce6 and IR825 were measured to be 3.8% and 10%, respectively, in the final product, IR825@C18PMH-PEG-Ce6 micelle nanoparticles. Via dynamic light scattering (DLS) measurement, it was found that when IR825 was encapsulated by C18PMH-PEG-Ce6, significant enlarged particle sizes were observed from ≈26 nm for the polymer itself, to ≈107 nm for the formed micelles (**Figure 1**a). Scanning electron microscopy (SEM) images also revealed that the formed IR825@C18PMH-PEG-Ce6 micelle nanoparticles exhibited uniform morphology and sizes with diameters of 100–200 nm (Figure 1b). The nanoparticle size observed from SEM appeared to be larger than that measured from DLS, probably due to the collapse of the nanoparticle on the silicon substrate under the dried condition. Due to the existence of excess carboxyl groups on Ce6, IR825@C18PMH-PEG-Ce6 micelles appeared to be negatively charged with a zeta potential at – 9 mV (Supporting Information Figure S2).

The formed IR825@C18PMH-PEG-Ce6 sample was highly stable in various physiological solutions, without showing significant release of Ce6 or IR825 even after 7 days incubation with PBS. UV–Vis–NIR absorbance spectra (Figure 1c) revealed the characteristic peaks of Ce6 (404 nm and 650 nm) for C18PMH-PEG-Ce6 polymer before and after IR825 encapsulation, as well as the IR825 peak (≈830 nm) in the IR825@C18PMH-PEG-Ce6 sample. As a result of the high NIR absorbance contributed by IR825, our IR825@C18PMH-PEG-Ce6 nano-micelles exhibited rapid temperature rise under irradiation by an 808-nm laser (Figure 1d), suggesting the great photothermal capacity of those polymeric nanoparticles.

Although it is well know that porphyrin and its derivatives can serve as chelating molecules to capture metal ions,[36,37] the

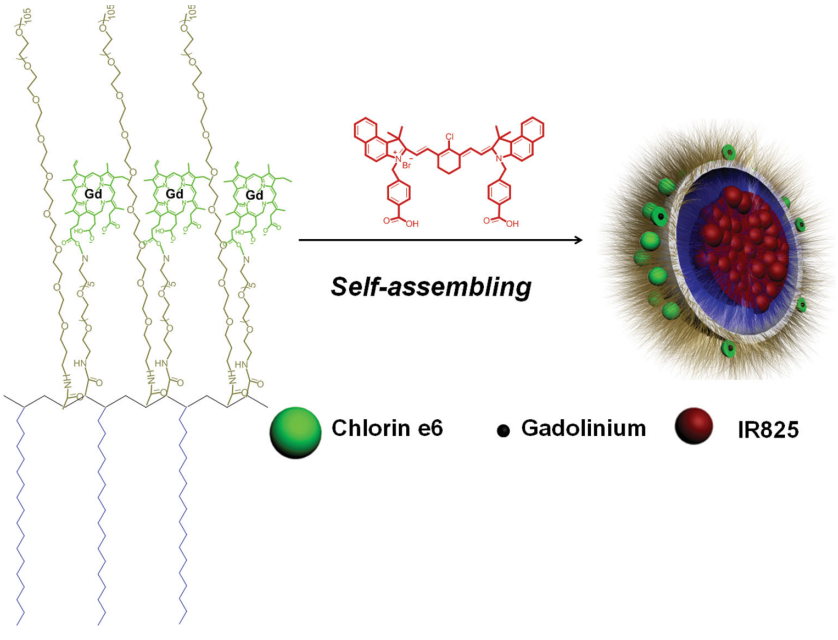

Scheme 1. A scheme showing the structure of IR825@C18PMH-PEG-Ce6-Gd nano-micelles. Ce6 is anchored on the backbone of C18PMH-PEG polymer via a short PEG linker. Gd^{3+} forms a chelate complex with Ce6. IR825, a water-insoluble NIR dye, is then encapsulated inside the formed nano-micelles.

© 2014 WILEY-VCH Verlag GmbH & Co. KGaA, Weinheim

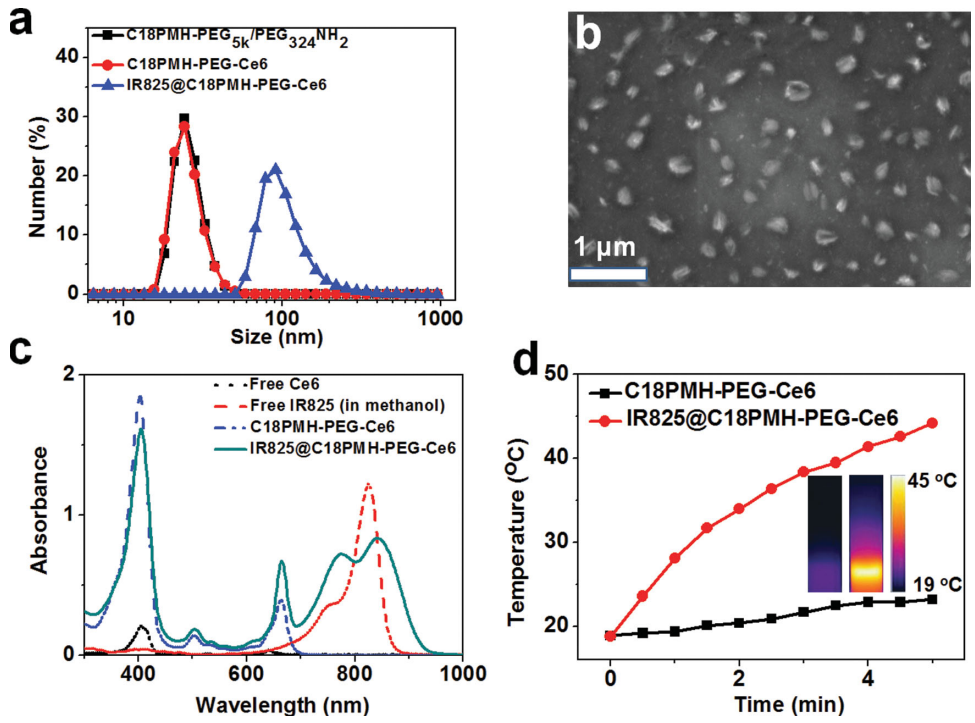

Figure 1. Characterization of IR825@C18PMH-PEG-Ce6-Gd nano-micelles. a) Hydrodynamic diameters of IR825@C18PMH-PEG-Ce6 after step-by-step synthesis. b) A SEM image of IR825@C18PMH-PEG-Ce6-Gd nanoparticles deposited on a silicon substrate. c) UV–Vis–NIR spectra of free Ce6, free IR825 (in methanol), C18PMH-PEG-Ce6, and IR825@C18PMH-PEG-Ce6. d) Heating curves of C18PMH-PEG-Ce6 and IR825@C18PMH-PEG-Ce6 with the equivalent Ce6 concentration at 0.1 mg/mL irradiated by the 808-nm laser at the power density of 0.3 W/cm^2.

use of metalloporphyrin as MR contrast agents has not yet been reported to our best knowledge. Here, we uncovered that Ce6 with a porphyrin ring could be used to chelate the commonly used T_1 weighted MR contrast agent, gadolinium-III (Gd^{3+}). The chelation of Gd^{3+} by Ce6 anchored on the C18PMH-PEG-Ce6 polymer occurred at a molar ratio of 1:1, as proven by our inductively coupled plasma atomic emission spectroscopy (ICP-AES) measurement of the sample after removal of unbound Gd^{3+} through dialysis. To explore the possibility of using IR825@C18PMH-PEG-Ce6-Gd as a T_1 weighted MR contrast agent, we measured its T_1 relaxation time as a function of Gd^{3+} concentration. The r_1 value for Ce6 chelated Gd^{3+} (Ce6-Gd) was measured to be only 1.95 mM^{-1} s^{-1}, which was lower than the clinical approved T_1 weighted contrast agent, Magnevist (4.29 mM^{-1} s^{-1}). However, the r_1 value of IR825@C18PMH-PEG-Ce6-Gd was dramatically enhanced to be 29.91 mM^{-1} s^{-1}, which was ≈7 times larger than Magnevist (**Figure 2**). Abundant macromolecules and nanoparticles have been used as platforms for gadolinium loading, such as dendrimers,[38,39] polymers,[40] liposomes,[41,42] as well as silicon nanoparticle[43,44]. The r_1 value of chelated Gd^{3+} is generally between 5 and 30 mM^{-1} s^{-1} when being integrated into nanocarrier systems as the result of increased local concentration of Gd^{3+} and lowered molecular tumbling rate in those Gd-containing complexes.[45–48] The high r_1 value of IR825@C18PMH-PEG-Ce6-Gd suggests its superior contrasting ability in T_1-weighted MR imaging.

The SO production abilities of free Ce6, Ce6-Gd, IR825@C18PMH-PEG-Ce6, and IR825@C18PMH-PEG-Ce6-Gd were then determined by a SO specific dye, singlet oxygen sensor green (SOSG). Although the SO production efficiency of Ce6 was slightly quenched after chelation with Gd^{3+}, no appreciable difference was observed between IR825@C18PMH-PEG-Ce6 and IR825@C18PMH-PEG-Ce6-Gd was observed (Figure S5b, Supporting Information). It is known that the longer triplet life time and higher triplet quantum yield of metal chelated phalocyanine, a derivative of porphyrin, can be obtained after complexing with diamagnetic irons, such as Al^{3+} and Zn^{2+}, compared to those complexing with paramagnetic transition metal irons, such as Cu^{2+}, Co^{2+}, and Gd^{3+}.[49] Therefore it is not a surprise to see the partially decreased SO production ability of Ce6 after being complexed with Gd^{3+}. Nevertheless, the largely retained SO generation ability of IR825@C18PMH-PEG-Ce6-Gd still allowed us to use those nano-micelles for photodynamic cancer treatment.

2.2. In Vitro Cell Experiments

In order to study the phototoxicity of IR825@C18PMH-PEG-Ce6 and IR825@ C18PMH-PEG-Ce6-Gd with Ce6 and Ce6-Gd, the relative viabilities of 4T1 cells with or without 660 nm light treatment after incubation with various concentrations of the above four agents were measured. All the four groups exhibited negligible cell toxicity under dark conditions (**Figure 3**a), while under 660-nm light exposure, the cell viabilities decreased as the increase of equivalent Ce6 concentrations, indicating the photosensitizer in four different forms were all active in photodynamic cancer cell killing.(Figure 3b). Interestingly, we found

© 2014 WILEY-VCH Verlag GmbH & Co. KGaA, Weinheim

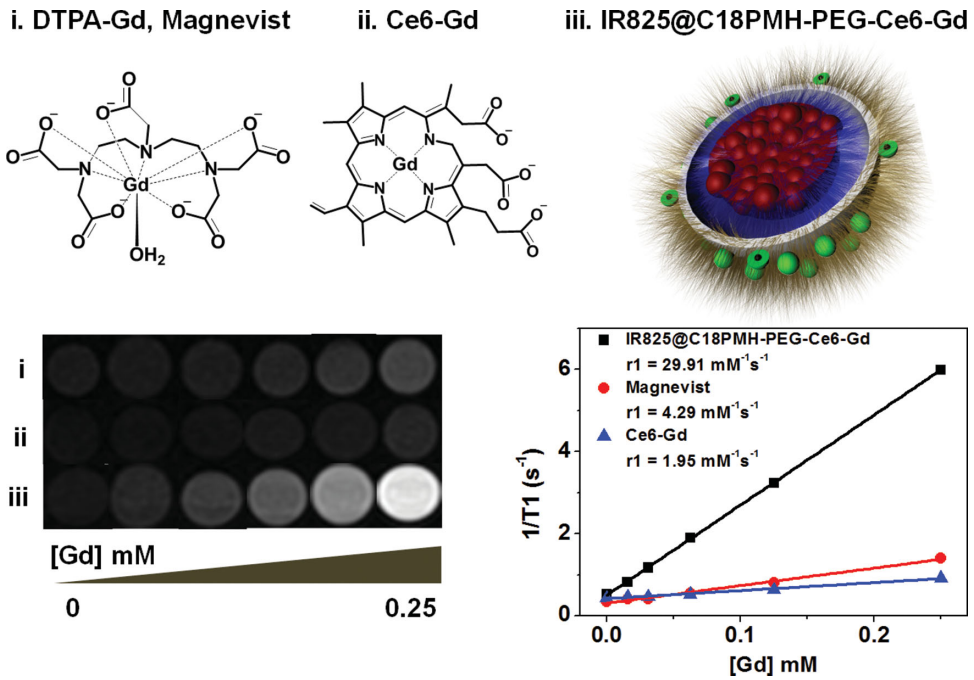

Figure 2. T_1 weighted MR images and T_1 relaxation rate of Magnevist (DTPA-Gd) (i), Ce6 chelated with gadolinium (Ce6-Gd) (ii), and IR825@C18PMH-PEG-Ce6-Gd (iii) measured at different gadolinium concentrations. IR825@C18PMH-PEG-Ce6-Gd showed a rather high r_1 relaxivity, which appeared to be ≈7 times higher than that of Magnevist, a clinically used agent.

that the two micelle forumulations, IR825@C18PMH-PEG-Ce6 and IR825@C18PMH-PEG-Ce6-Gd, showed significantly enhanced phototoxicity when compared with the free forms, Ce6 and Ce6-Gd. Such observation apparently could not be explained by the SO generation abilities of those agents. We thus wondered whether the nanoparticle formulation could facilitate the cellular uptake of photosensitizers. From the flow cytometry data in Supporting Information Figure S4a–d and Figure 3c, the cellular fluorescence intensity of Ce6 for both IR825@C18PMH-PEG-Ce6 and IR825@C18PMH-PEG-Ce6-Gd treated cells were about 20 times higher than those incubated with free Ce6 and Ce6-Gd, even though the Ce6 fluorescence was partially quenched by ~50% in the polymeric micelle formulations (Figure S5a, Supporting Information). Those data clearly evidenced that Ce6 in the nanoparticle form exhibited remarkably enhanced cellular uptake, which resulted in the enhanced in vitro photodynamic efficacy of IR825@C18PMH-PEG-Ce6 and IR825@C18PMH-PEG-Ce6-Gd.

The combined effect of photothermal and photodynamic therapy was then studied in vitro. 4T1 cells were incubated with various concentrations of IR825@C18PMH-PEG-Ce6-Gd for 6 h, after which PDT (660-nm, 2 mW/cm^2, 10 min), PTT (808-nm, 0.5 W/cm^2, 5 min), PDT+PTT, as well as PTT+PDT treatments were conducted. It was found that single treatment by either PDT or PTT could only induce partial cell death at the current conditions. In marked contrast, the combination treatments, regardless of the sequence of PDT and PTT, were found to be highly effective in destructing cancer cells. The live and dead double cell staining results in Figure 3e also intuitively evidenced the synergistic effects of combined PDT and PTT. While the dead cells (Propidium Iodide, PI, red) were predominant in combination treatment groups, the proportion of live cells (Calcein AM, green) prevailed over that of dead cells for the single PTT or PDT treatment group. Notably, we found that the sequence of PTT and PDT exerted no obvious effect to the in vitro therapeutic efficacy.

2.3. Triple-Modal Imaging

Multimodal imaging that integrates multiple modalities into a single nanocarrier system is advantageous compared with single modal imaging,[43,50–53] as each imaging modality has its respective advantages and drawbacks.[17,54,55] In our study, IR825@C18PMH-PEG-Ce6-Gd could serve as a multifunctional agent that offers contrast in three different modalities: fluorescence imaging, MR imaging, and photoacoustic tomography (PAT).

In vivo fluorescence imaging was conducted by recording Ce6 fluorescence at different time points after injection of IR825@C18PMH-PEG-Ce6-Gd. The fluorescence signals distributed extensively in all parts of the mice body within 1 h post-injection (p.i.), likely due to the high concentration of the micelles in blood vessels. Afterwards, the fluorescence signals of the tumor increased and reached to a peak value at 4 hours p.i. (**Figure 4**a,c), suggesting the gradual accumulation of nanoparticles in the tumor. The tumor to normal tissue (T/N) signal ratio was measured to determine the optimal time window for subsequent therapy. It was found that at 12 h p.i., the T/N ratio reached its peak and maintained at that level subsequently (Figure 4c).

To understand the observed high tumor uptake of nanoparticles, the blood circulation of IR825@C18PMH-PEG-Ce6-Gd after i.v. injection into mice ([Ce6] = 0.6 mg/ml)

© 2014 WILEY-VCH Verlag GmbH & Co. KGaA, Weinheim

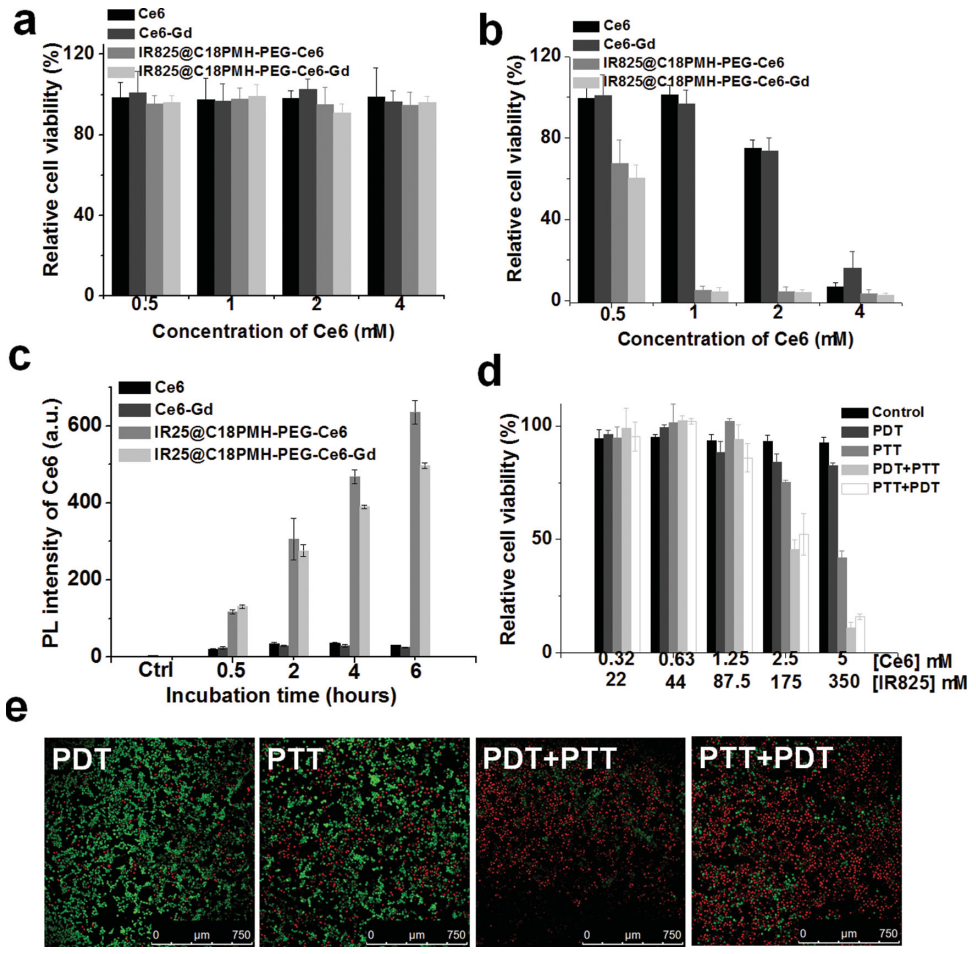

Figure 3. In vitro PDT and combination therapy. a,b) Relative viabilities of 4T1 cells treated by Ce6, Ce6-Gd, IR825@C18PMH-PEG-Ce6, and IR825@C18PMH-PEG-Ce6-Gd a) without or b) with 660 nm light exposure at the power density of 2 mW/cm^2 for 30 min. c) Cellular fluorescence intensity of Ce6 measured by flow cytometry after incubation with Ce6, Ce6-Gd, IR825@C18PMH-PEG-Ce6, and IR825@C18PMH-PEG-Ce6-Gd ([Ce6] = 4 μM) as a function of incubation time. d) Relative viabilities of 4T1 cells for different treatment groups after being incubated with IR825@C18PMH-PEG-Ce6-Gd with different concentrations. PDT was introduced by 660-nm light irradiation at 2 mW/cm^2 for 10 min, while PTT was conducted by 808-nm laser irradiation at 0.5 W/cm^2 for 5 min. e) Confocal fluorescence microscope images of Calcein AM and PI co-stained 4T1 cells after various treatments indicated. Green and red colors represented live and dead cells, respectively. Note that the PDT optical dose used in combination therapy (d,e) was only 1/3 of that used in (b).

was determined through the measurement of Ce6 fluorescence. The first and second phases of circulation half-lives were calculated to be 1.34 ± 0.23 h and 23.69 ± 3.63 h respectively by secondary exponential fitting (Figure S6, Supporting Information), suggesting the stealth-like behavior of those polymeric micelles after i.v. injection in the blood. Such a long blood circulation half-life is greatly desired for tumor passive targeting as nanoparticles could repeatedly pass through tumor vasculatures and got trapped inside the tumor as a result of the well-known enhanced permeability and retention (EPR) effect of cancerous tumors.[56]

Those mice were then sacrificed at 24 h p.i., with major organs taken for ex vivo imaging. Based on the fluorescence of Ce6, the tumor was found to be the brightest among all the organs, suggesting high tumor uptake efficacy of those nanoparticles (Figure S7a, Supporting Information). To understand the biodistribution of nanoparticle in a more quantitative manner, the harvested organs of mice were homogenized by a lysis buffer. The fluorescence of Ce6 in those tissue lysates was measured to determine the accumulation of nanoparticles. Different from ex vivo imaging data, the tumor uptake of nanoparticles, although quite high, appeared to be lower than that in the liver (Figure S7b, Supporting Information). Such inconsistency might be attributed to the fluorescence quenching of Ce6 by its complicated surrounding biological molecules and tissues when it is retained inside certain organs. Nevertheless, our results still evidenced the rather efficient tumor passive uptake of our theranostic nanoparticles.

With a rather high r_1 value, we thus used IR825@C18PMH-PEG-Ce6-Gd for T_1-weighted MR imaging. Figure 4b showed the cross-section T_1 MR images of mice acquired at different time intervals after injection. The brighten T_1 MR signals in the tumor appeared early at one hour p.i. and gradually reached the plateau after 3 hours. Different with fluorescence imaging based on Ce6 fluorescence, which showed a decreased tumor signals later on, the MR signals in the tumor remained

© 2014 WILEY-VCH Verlag GmbH & Co. KGaA, Weinheim

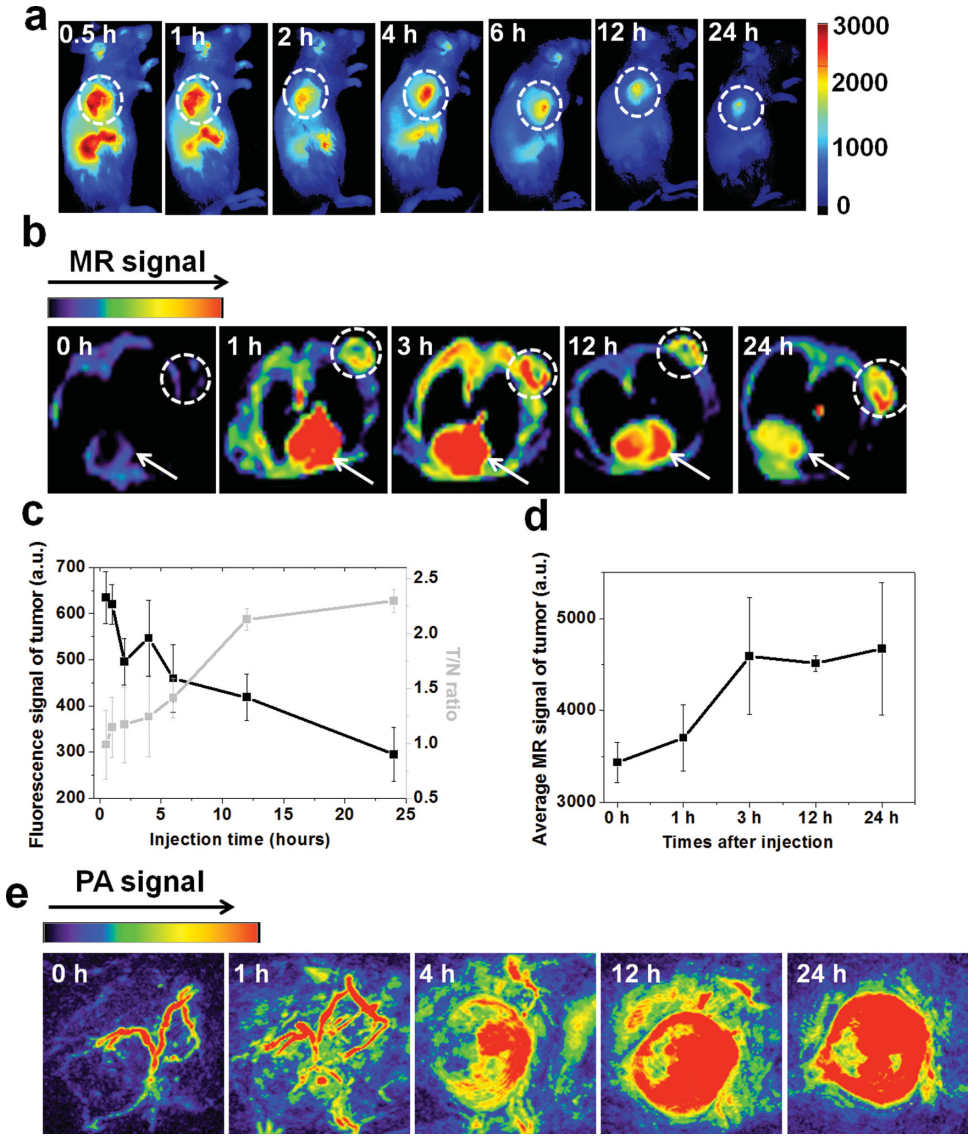

Figure 4. In vivo triple-modal imaging. a) In vivo fluorescence and b) MR imaging of 4T1 tumor-bearing mice taken at different time points post i.v. injection of IR825@C18PMH-PEG-Ce6-Gd at the same dose (200 μL, [Ce6] = 0.5 mg/mL, [IR825] = 1.3 mg/mL). Dashed circles in (a) and (b) highlight the tumor, while arrows in (b) point to the heart. c) The quantification of tumor signals and tumor / normal tissue signal (T/N) ratios from fluorescent images shown in (a) at different post-injection time. d) The quantification of average T_1-MR signals in the tumor by manual drawn region of interest at different post-injection time. e) In vivo photoacoustic imaging of 4T1 tumor-bearing mice taken at different time points after i.v. injection with IR825@C18PMH-PEG-Ce6-Gd.

stable after 3 hours (Figure 4d). Again such discrepancy may be explained by the fluorescence quenching effect of Ce6 over time in the mouse body.

Apart from tumor imaging, this contrast agent appeared to be useful for blood pool imaging as heart could be clearly visualized under MR imaging after injection of IR825@C18PMH-PEG-Ce6-Gd (Figure 3b). The MR signals in the mouse heart decreased over time owing the gradual clearance of nanoparticles from blood circulation, but remained clearly visible even after 24 h. Note that blood pool imaging with Magnevist (Gd-DTPA) as the contrast agent could only be conducted right after injection because of the rapid clearance and rather short blood circulation half-life of Magnevist.

Photoacoustic imaging tomography (PAT) is a newly emerged modality which relies on the absorption of light and emission of the wide band ultrasound for detection of light-absorbing tissues. Compared with traditional optical imaging, PAT shows greatly improved tissue penetration depth and enhanced in vivo spatial resolution. With strong NIR absorbance attributed from IR825, IR825@C18PMH-PEG-Ce6-Gd could also offer contrast in PAT imaging. In addition to fluorescence and MR imaging, PA images were also taken at various time points after i.v. injection of IR825@C18PMH-PEG-Ce6-Gd (Figure 4e). Before injection of our nano-agent, only large blood vessels could be visualized under PAT imaging owing to the endogenous light absorption by hemoglobin in the blood.

© 2014 WILEY-VCH Verlag GmbH & Co. KGaA, Weinheim

After injection of our IR825-containing micelles, the PA signal in tumor tissue get stronger over time due to the passive tumor accumulation of nanoparticles. The whole tumor was lighten up at later time points, indicating that those nanoparticles were homogenously distributed inside the tumor.

Therefore, triple modal fluorescence, MR, and PAT imaging was realized using IR825@C18PMH-PEG-Ce6-Gd as the contrast agent in our study. Fluorescence imaging is a quite sensitive modality for superficial tumor imaging, however its reliability sometimes may be affected by the quenching of fluorescence molecules in the complicated biological tissues. Although MR imaging enables whole-body imaging without the tissue depth limit (e.g., tumor imaging and blood pool imaging at the same time), its sensitivity and spatial resolution could be its limitations. On the other hand, PAT imaging, which is difficult for whole-body imaging, exhibits high in vivo imaging spatial resolution and could illustrate the detailed distribution of nanoparticles inside the tumor. Those three imaging modalities with their respectively advantages and limitations taken together could provide valuable information for planning and guiding therapeutic actions.

2.4. In Vivo Combination Therapy

Encouraged by the triple-modal imaging data, which revealed the rather effective and homogenous tumor uptake of our theranostic nanoparticles, we then would like to use IR825@C18PMH-PEG-Ce6-Gd for in vivo cancer treatment. The in vivo photothermal effect was firstly studied. Rapid temperature rise was observed on the tumors of injected mice under 808-nm laser irradiation at a power density of 0.3 W/cm^2, while no obvious temperature change for the control group was noted, demonstrating the possibility of using IR825@C18PMH-PEG-Ce6-Gd as a photothermal agent for in vivo cancer treatment. (**Figure 5**a,b)

For our cancer treatment experiment, mice bearing 4T1 tumors with initial volumes of 100–150 mm^3 were chosen and randomly divided into 5 groups, with one group injected with saline as a control and the other 4 groups injected with IR825@C18PMH-PEG-Ce6-Gd (200 µL, [Ce6] = 0.5 mg/mL, [IR825] = 1.3 mg/mL). 12 h after injection, the corresponding treatments were conducted. For the PTT treatment, the mice were irradiated with 808-nm laser at the power density of 0.3 W/cm^2 to keep the tumor temperature at 49 °C for 6 min, while the mice for the PDT treated group were irradiated with 660-nm light at the power density of 2 mW/cm^2 for 1 h. Tumor volumes and body weights were monitored every other day. For tumors after only PTT treatment, their growth was largely inhibited in the first 8 days, after which, however, rapid regrowth occurred later on. The tumor growth in the PDT treated group was also only partially inhibited. In marked contrast, both the "PDT+PTT" treatment and "PTT+PDT" treatment could greatly inhibit the growth of tumors after treatments (Figure 5c). The therapeutic efficacies in these two groups showed no significant difference, suggesting that the sequence of PTT and PDT was not an important issue in the combination therapy. Moreover, neither obvious body weight loss nor noticeable abnormality was found

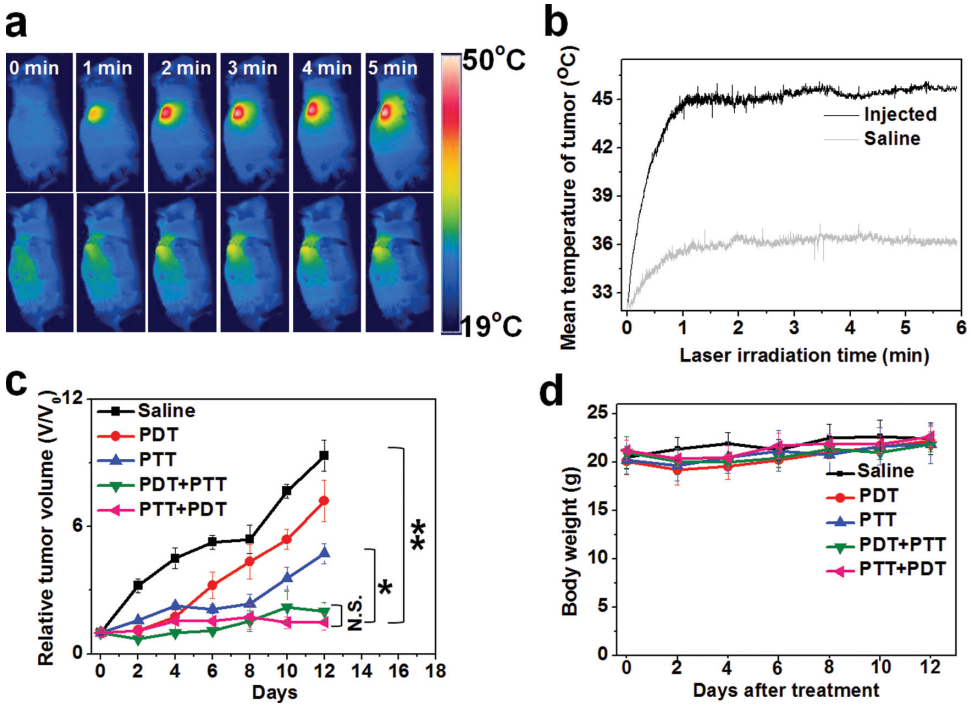

Figure 5. In vivo combination therapy. a) IR thermal images of 4T1 tumor-bearing mice under 808 nm laser irradiation (0.3 W/cm^2) after i.v. injection of IR825@C18PMH-PEG-Ce6-Gd (200 µl, [Ce6] = 0.5 mg/mL, [IR825] = 1.3 mg/mL) (Upper row) and saline (lower row). b) Tumor temperature change of mice monitored by the IR thermal camera during laser irradiation as indicated in (a). c) Tumor growth curves of different groups of mice after various treatments indicated (5 mice per group). Error bars were based on standard error of mean (SEM). (N.S. no significance, *$p < 0.05$, **$p < 0.01$). d) Body weight data of mice after various treatments indicated.

© 2014 WILEY-VCH Verlag GmbH & Co. KGaA, Weinheim

in the four groups of mice (Figure 5d), indicating no significant acute toxicity of our theranostic agent.

In order to further understand the therapeutic effects after various treatments down to the cellular level, both the hematoxylin and eosin (HE) staining and terminal deoxynucleotidyl transferase dUTP nick end labeling (TUNEL) assays were introduced to study the morphology and apoptosis of tumor cells, respectively. Considering the limited penetration depth for light, we compared the superficial and deep regions of tumor slices for the five groups 7 days after treatments (**Figure 6**). Based on HE and TUNEL staining results, necrosis and apoptosis of tumor cells could be observed in the superficial regions of tumors in the PDT treated group, but only to a small extend. The inner part of the tumor after only PDT treatment was essentially intact. For tumors after PTT treatment, although severe apoptosis and necrosis were found in the superficial region, the majority of cells remained viable in the deeper regions, which would become the seed for the tumor regrowth. Therefore, either PDT or PTT at the current low dose was not able to effectively kill tumors, particular their deep parts. Unlike single treatment groups, the combination therapy resulted in high degrees of tumor cell necrosis and apoptosis in both the superficial and deep tumor tissues, showing a synergistic effect that was in accordance with the tumor volume growth data. The limited penetration depth of light is the major impediment for treating deeper tumor tissues in phototherapy. The synergistic effect of PDT and PTT, which could be effective under much lower optical doses, is thus useful to kill deep tumor cells located far from the skin, though the light power density at that region has been significantly attenuated.

Thus, we have realized a synergistic effect in the combined photodynamic and photothermal therapy of cancer using IR825@C18PMH-PEG-Ce6-Gd as a multifunctional theranostic agent. In our experiment, the single treatment with either PDT or PTT could hardly inhibit the tumor growth unless increasing the injection dosage, laser power density or irradiation time, which would lead to the risk of overtreatment. Though the two types of treatments have different mechanisms as PTT relies on the physical heating to "boil" the tumor, while PDT takes advantages of singlet oxygen production, they may probably exert some positive effects on each other. Several groups, including ours, have proven that the mild photothermal heating could accelerate the cellular uptake of nano-carriers to enhance the delivery of either chemotherapeutic drugs or photosensitizers[32]. On the other hand, it has been speculated that the photodynamic treatment might enhance the sensitivity of tumor cells to heat, although the detailed mechanism merits further investigation.[28]

Regarding the sequence of PDT and PTT, two major hypotheses have been proposed based on different mechanisms. A number of studies have found that PDT followed after PTT could offer better therapeutic outcomes than the reversed approach, as the photothermal effect in their systems could either trigger the release of photosensitizers from their carriers or enhance the cellular uptake of the nano-carriers.[26,27] In contrast, others have also shown that the photothermal effect could damage photosensitizers, thus "PDT + PTT" is preferred over "PTT + PDT".[28] In our cases, photosensitizer was covalently anchored on the polymer backbone and thus could hardly be released from their carrier in the existence of the photothermal effect. Furthermore, we also compared the SO production of IR825@C18PMH-PEG-Ce6-Gd before and after photothermal treatment (0.3 W/cm^2, 6 min) and observed no significant difference (data not shown), probably owing to the relatively mild photothermal heating parameters used in our experiments. Therefore, while both "PDT+PTT" and "PTT+PDT" can effectively inhibit tumor growth with synergist effects, the sequence of PDT and PTT in our system is not an important factor to determine the final treatment outcomes.

3. Conclusions

In summary, we have successfully fabricated a novel class of polymer-based theranostic agent, namely polymeric micelles

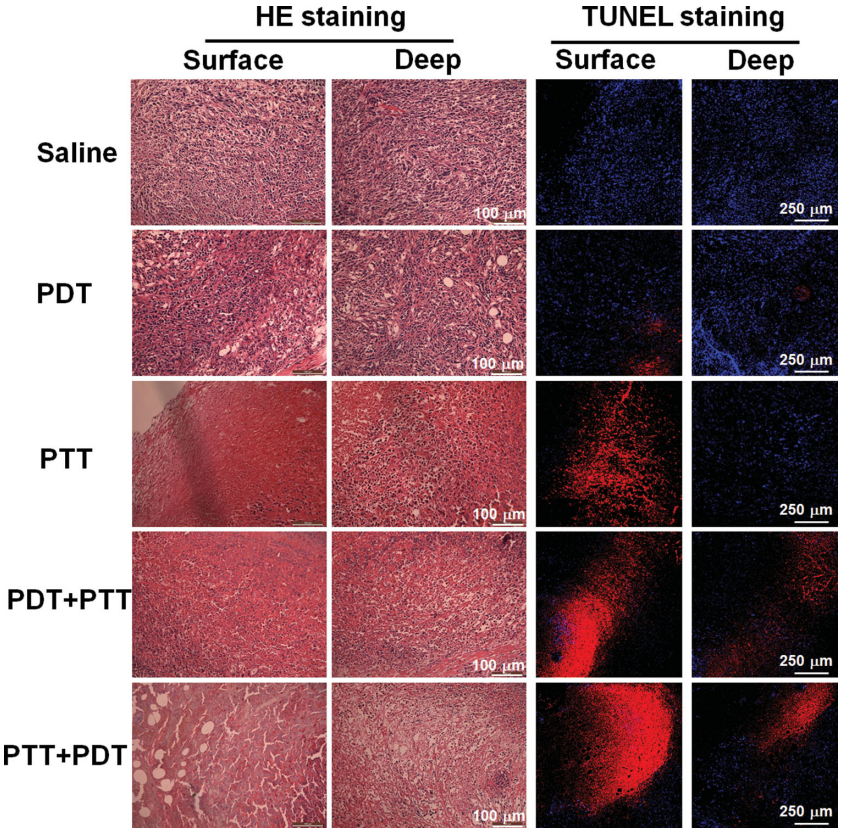

Figure 6. Histological examination of tumor after various treatments indicated. Left: HE staining of superficial region and deep region of the tumor. Right: TUNEL staining of superficial region and deep region of the tumor. Significantly enhanced damage occurred in the deep region of the tumor after the combination therapy was conducted.

© 2014 WILEY-VCH Verlag GmbH & Co. KGaA, Weinheim

of IR825@C18PMH-PEG-Ce6-Gd, which could be used for multimodal imaging guided combination therapy of cancer. In this system, we for the first time uncover that Ce6, a porphin-based photosensitizer, could form a chelate with Gd^{3+} to allow T_1-weighted MR imaging. The r_1 relaxivity of the IR825@C18PMH-PEG-Ce6-Gd formulation is found to be 7 times higher than that of Magnevist, a clinical Gd-based T_1-weighted contrast agent. While the SO production of Ce6 is well maintained after being anchored on the polymer backbone and complexed with gadolinium, the obtained nano-micelles could facilitate the cellular uptake of photosensitizer to allow more effective photodynamic cell killing, which is further enhanced with photothermal heating. In our animal experiments, triple-modal fluorescence, MR and photoacoustic imaging is conducted, and reveals the efficient and homogenous uptake of nanoparticles in the tumor. Combined photodynamic and photothermal therapy is finally carried out, achieving a remarkable synergist effect in inhibiting tumor growth, regardless of the sequence of PDT and PTT. As illustrated by HE and TUNEL staining assay, while only the superficial region of the tumor is affected by single PDT or PTT, the combined treatment could damage both superficial and deep regions of the tumor under mild optical doses (7.2 J/cm^2 for PDT and 108 J/cm^2 for PTT), which are rather low compared to those used in other PDT or PTT studies.[9,27,28,57] Compared with many other inorganic-based theranostic agents, the polymer-based ones as presented in this work may have much less safety concern and fewer obstacles towards future clinical uses. While multimodal imaging could be beneficial in cancer diagnosis, therapeutic planning, and post-treatment prognosis, the combination therapy would then offer improved therapeutic efficacy without raising the risk of over-treatment. Therefore, the multifunctional nano-micelles developed in this work may be of great promise in cancer theranostics.

4. Experimental Section

Synthesis of IR825@ C18PMH-PEG-Ce6-Gd: 5 kDa PEG drafted poly(maleic anhydride-alt-1-octadecene) (C18PMH-PEG_{5k}) was synthesized following the protocol reported previously.[58] Briefly, 10 mg poly(maleic anhydride-alt-1-octadecene) (C18PMH, Sigma-Aldrich) was mixed with 143 mg mPEG_{5k}-NH_2 (JiaXingBoMei, China) in 3 mL dichloromethane to render a transparent solution. After adding 6 µL triethylamine (TEA), the solution was stirred for overnight. Then 6 mg *N*-(3-Dimethylaminopropyl)-*N*'-ethylcarbodiimide hydrochloride (EDC, Sigma-Aldrich) was added to the above solution and reacted for 24 h. To anchor diamino small molecular PEG (NH_2-PEG_{324}-NH_2, Mw = 324.23) to the backbone of C18PMH-PEG_{5k}, 93 mg NH_2-PEG_{324}-NH_2 and 8.2 mg EDC predissolved in 2 mL dichloromethane (DMF) was added to the above solution. After stirring for 24 h, the above solution was dialyzed against water by a 14 KDa cut-off membrane, and lyophilized to render C18PMH-PEG_{5k}/$PEG_{324}NH_2$ polymer. For Ce6 conjugation, 17 mg chlorin e6 (Ce6, Sunbio, USA) was mixed with 11 mg EDC in 1 mL DMF, and reacted for 1 hour before being added to the 140 mg of synthesized C18PMH-PEG_{5k}/$PEG_{324}NH_2$ predissolved in 2 mL DMF with 200 µL TEA. After reaction for 24 h, the above solution was dialyzed against water by a 14 KDa cut-off membrane and then lyophilized to render C18PMH-PEG-Ce6. All polymers obtained at each step were analyzed by ^{1}H nuclear magnetic resonance (NMR). Finally, for the loading of IR825, which was synthesized according to our previously reported protocol,[35] 10 mg IR825 was dissolved in 1 mL methanol containing 200 µL TEA to get a transparent dark green solution, which was then mixed with 100 mg C18PMH-PEG-Ce6 predissolved in 2 mL methanol. The solution was dialyzed against water by a 14 KDa cut-off membrane and stored at 4 °C for future use. To chelate gadolinium with Ce6 molecules anchored at the polymers, gadolinium chloride ($GdCl_3$) was added to the solution containing C18PMH-PEG-Ce6 at a molar ratio of 2:1 ($GdCl_3$: Ce6). The excess $GdCl_3$ was removed through dialysis.

Characterization of the Polymers: The SEM images were obtained by using a scanning electron microscopy (SUPRA 55, Carl Zeiss). UV–Vis–NIR spectra were recorded by using Genesys 10s UV–Vis–NIR spectrophotometer (Thermo scientific, USA). Fluorescence spectra were acquired on a FluoroMax 4 luminescence spectrometer (HORIBA, Jobin Yvon). The sizes of micelle nanoparticles were measured using ZEN3690 zetasizer (Malvern, USA). The concentration of Gd in Ce6-Gd, DTPA-Gd (Magnevist), and IR825@C18PMH-PEG-Ce6-Gd samples were measured by inductively coupled plasma atomic emission spectroscopy (ICP-AES). IR825@C18PMH-PEG-Ce6-Gd solutions with different Gd concentrations ranging from 0.012 mM to 0.25 mM were scanned under a 3.0 T clinical MR scanner (GE Healthcare, USA) at room temperature. After acquiring the T_1-weighted MR images, the signal intensity of each sample was measured by drawing regions-of-interest. By plotting the r_1 value ($1/T_1$) for each sample against the Gd concentration, the final r_1 value for IR825@ C18PMH-PEG-Ce6-Gd was calculated by curve fitting. The method for the singlet oxygen detection was based on the protocol reported previously.[59] In brief, 100 mg singlet oxygen sensor green reagent (SOSG, molecular probes, USA) was dissolved in 330 mL methanol to obtain the stock solution of SOSG (0.5 mM). Then 10 µL SOSG was added to 1990 µL sample solution of free Ce6, Ce6-Gd, IR825@C18PMH-PEG-Ce6, or IR825@ C18PMH-PEG-Ce6-Gd ([Ce6] = 1 µM). The four different samples were irradiated by a lamp equipped with a 660-nm band-pass filter at the power density of 2 mW/cm^2. The fluorescence intensity of SOSG was measured under the excitation wavelength of 494 nm. Error bars were based on triplicated samples.

Cell Related Experiments: 4T1 murine breast cancer cells were originally purchased from American Type Culture Collection (ATCC) and cultured in RPMI-1640 cell medium supplemented with 10% fetal bovine serum (FBS) and 1% penicillin/streptomycin under 37 °C within 5% CO_2. Standard thiazolyl tetrazolium (MTT, Sigma-Aldrich) tests were used to evaluate the photodynamic effects of the various materials. The cells were pre-seeded into 96-well plates at the density of 1×10^4 per well. A series concentrations of Ce6 (0.5, 1, 2, 4 µM) in four different forms, including free Ce6, Ce6 chelated with Gd (Ce6-Gd), IR825@C18PMH-PEG-Ce6, and IR825@C18PMH-PEG-Ce6-Gd, were added. After 6 hours of incubation, one group of cells were directly irradiated by the 660-nm light at the power density of 2 mW/cm^2 for 30 min, while the other group of cells were remained in dark. All the cells were allowed to be incubated for another 24 h before the standard MTT test was conducted. To determine the cellular uptake efficiencies, 4T1 cells pre-seeded in 24-well plates at the density of 5×10^4 cells/well were incubated with free Ce6, Ce6-Gd, IR825@C18PMH-PEG-Ce6, and IR825@C18PMH-PEG-Ce6-Gd at a Ce6 equivalent concentration of 4 µM for different periods of time (0.5, 2, 4, 6 h). After washing cells with PBS for 3 times, the cellular Ce6 fluorescence was analyzed by flow cytometry (FACS Calibur from Becton, Dickinson Company) using a 633 nm laser as an excitation source. For the combined photothermal and photodynamic therapy at the cellular level, 4T1 cells in 96-well plates at the density of 1×10^4 cells/well were incubated with different concentrations of IR825@C18PMH-PEG-Ce6-Gd for 6 hours. Afterwards cells of the PTT group were irradiated by an 808-nm laser for 5 min at the power density of 0.5 W/cm^2, while cells of the PDT group were irradiated by 660-nm light for 10 min at the power density of 2 mW/cm^2. After incubation for 24 h, the standard MTT test was conducted to determine the relative viability of cells. For the co-staining of live and dead cells, cells pre-seeded in 35 mm plates at the density of 1×10^6 cells/plate were incubated with IR825@C18PMH-PEG-Ce6-Gd with a Ce6 equivalent concentration of 5 µM and a IR825 equivalent concentration of 350 µM. Six h after incubation, various treatments, including PTT, PDT, PDT+PTT, and PTT+PDT, were

© 2014 WILEY-VCH Verlag GmbH & Co. KGaA, Weinheim

conducted as described above. Cells were further incubated for 12 hours before co-staining. The dye solution was prepared by adding 10 μL 1 mmol/L calcein AM and 15 μL 1.5 mmol/L propidium iodide (PI) to 5 mL cell medium. Then 1 mL dye solution was added to each plate and incubated for 30 minutes at 37 °C. Finally, the cells were washed by PBS for 3 times to remove the excess dye solution and imaged by the Leica SP5 Confocal microscopy system (Calcein AM l_{ex} = 488 nm, l_{em} = 515 nm; PI l_{ex} = 535 nm, l_{em} = 617 nm).

Animal Model: Female Balb/c mice were purchased from Nanjing Peng Sheng Biological Technology Co. Ltd. and used under protocols approved by Soochow University Laboratory Animal Center. 4T1 cells (1×10^6) suspended in 50 mL PBS were subcutaneously injected into the flank of each mouse. After about 6 days, mice with tumor volumes at about 100–150 mm^3 were treated subsequently.

In Vivo Imaging: For in vivo imaging, 200 μL IR825@C18PMH-PEG-Ce6-Gd with a 0.5 mg/mL Ce6 equivalent concentration was intravenously (i.v.) injected into each mouse. In vivo fluorescence imaging was conducted using the Maestro in vivo fluorescence imaging system (CRi inc.). The autofluorescence was removed by the spectrum unmixing software. MR imaging was conducted by using a 3.0-T clinical MRI scanner (GE healthcare, USA) equipped with a special coil for small animal imaging. After acquiring T_1-weighted MR images, the signal intensity was measured within a manually drawn region of interest for each mouse. In vivo PA imaging was performed with a preclinical photoacoustic computerized tomography scanner (Endra Nexus 128, Ann Arbor, MI).

In Vivo Combination Therapy: Mice bearing 4T1 tumors were randomly divided into 5 groups (n = 5 per group). The control group of mice were i.v. injected with 200 μL of saline, while the rest four groups of mice were i.v. injected with 200 μL of IR825@C18PMH-PEG-Ce6-Gd ([Ce6] = 0.5 mg/mL, [IR825] = 1.3 mg/mL). 12 hours after injection, PTT, PDT, and the combination therapy were conducted. For the PTT group, the tumors were irradiated with the 808-nm laser at a power density of 0.3 W/cm^2. The temperatures of the tumor site were monitored through an IR thermal camera (Infrared Cameras Inc.). For the PDT group, the tumors were irradiated with the 660-nm light at a power density of 2 mW/cm^2 for 1 h. For the PDT plus PTT group, the mice were firstly exposed to the 660-nm light for 1 h, and then irradiated with the 808-nm laser. For the PTT plus PDT group, the mice were firstly irradiated with the 808 nm-laser, and then exposed to the 660-nm light. After various treatments, the tumor sizes and body weights were monitored every two days for 12 days. The tumor volume was calculated according to the following equation: width^2 x length/2.

Histological Examination: Hematoxylin and Eosin (HE) staining and Terminal Deoxynucleotidyl Transferase dUTP nick end labeling (TUNEL) assays were used to stain the tumor slices. For HE staining, tumor tissues from each group were harvested, fixed in 10% neutral buffered formalin, processed into paraffin, sectioned at 8 μm thickness, stained with hematoxylin and eosin (H&E), and examined by a digital microscope (Leica QWin). For TUNEL assay, the tumor tissue were cut into 10 μm slices after frozen in optimum cutting temperature (OCT) compound (SACURA, USA) medium. The fluorescent TUNEL staining was then conducted following manual instruction of In situ Cell Death Detection kit (Roche, Indianapolis, IN).

Acknowledgements

This work was partially supported by the National Basic Research Programs of China (973 Program) (2012CB932600, 2011CB911002), the National Natural Science Foundation of China (51222203, 51132006), the Natural Science Fund for Distinguished Young Scholars of Jiangsu Province, and a Project Funded by the Priority Academic Program Development (PAPD) of Jiangsu Higher Education Institutions. The authors thank Prof. Gang Liu for photoacoustic imaging and Yinan Zhong for her kind help in analyzing the ^{1}HNMR spectrum of the polymers.

Received: May 5, 2014
Revised: June 29, 2014
Published online: August 15, 2014

[1] S. Bown, *World J. Surg.* **1983**, *7*, 700.
[2] X. Huang, I. H. El-Sayed, W. Qian, M. A. El-Sayed, *J. Am. Chem. Soc.* **2006**, *128*, 2115.
[3] T. J. Dougherty, C. J. Gomer, B. W. Henderson, G. Jori, D. Kessel, M. Korbelik, J. Moan, Q. Peng, *J. Natl. Cancer Inst.* **1998**, *90*, 889.
[4] S. Nie, *Nanomedicine* **2010**, *5*, 523.
[5] J. Xie, S. Lee, X. Chen, *Adv. Drug Delivery Rev.* **2010**, *62*, 1064.
[6] T. Lammers, S. Aime, W. E. Hennink, G. Storm, F. Kiessling, *Acc. Chem. Res.* **2011**, *44*, 1029.
[7] S. Chapman, M. Dobrovolskaia, K. Farahani, A. Goodwin, A. Joshi, H. Lee, T. Meade, M. Pomper, K. Ptak, J. Rao, *Nano Today* **2013**, *8*, 454.
[8] M. W. Ambrogio, C. R. Thomas, Y.-L. Zhao, J. I. Zink, J. F. Stoddart, *Acc. Chem. Res.* **2011**, *44*, 903.
[9] Z. Li, C. Wang, L. Cheng, H. Gong, S. Yin, Q. Gong, Y. Li, Z. Liu, *Biomaterials* **2013**, *34*, 9160.
[10] Z. Li, S. Yin, L. Cheng, K. Yang, Y. Li, Z. Liu, *Adv. Funct. Mater.* **2013**.
[11] X. Song, H. Gong, S. Yin, L. Cheng, C. Wang, Z. Li, Y. Li, X. Wang, G. Liu, Z. Liu, *Adv. Funct. Mater.* **2013**, *24,* 1194.
[12] K. Yang, L. Hu, X. Ma, S. Ye, L. Cheng, X. Shi, C. Li, Y. Li, Z. Liu, *Adv. Mater.* **2012**, *24*, 1868.
[13] G. von Maltzahn, J.-H. Park, A. Agrawal, N. K. Bandaru, S. K. Das, M. J. Sailor, S. N. Bhatia, *Cancer Res.* **2009**, *69*, 3892.
[14] L. A. Yannuzzi, J. S. Slakter, N. E. Gross, R. F. Spaide, D. L. Costa, S. J. Huang, J. M. Klancnik Jr., A. Aizman, *Retina* **2003**, *23*, 288.
[15] Q. Tian, J. Hu, Y. Zhu, R. Zou, Z. Chen, S. Yang, R. Li, Q. Su, Y. Han, X. Liu, *J. Am. Chem. Soc.* **2013**, *135*, 8571.
[16] T. J. Vogl, K. Eichler, R. Straub, K. Engelmann, S. Zangos, D. Woitaschek, M. Böttger, M. G. Mack, *Eur. J. Ultrasound* **2001**,*13*, 117.
[17] S. M. Janib, A. S. Moses, J. A. MacKay, *Adv. Drug Delivery Rev.* **2010**, *62*, 1052.
[18] W. Zhang, Z. Guo, D. Huang, Z. Liu, X. Guo, H. Zhong, *Biomaterials* **2011**, *32*, 8555.
[19] H. Liu, D. Chen, L. Li, T. Liu, L. Tan, X. Wu, F. Tang, *Angew. Chem.* **2011**, *123*, 921.
[20] X. Ma, H. Tao, K. Yang, L. Feng, L. Cheng, X. Shi, Y. Li, L. Guo, Z. Liu, *Nano Res.* **2012**, *5*, 199.
[21] C. Wang, H. Xu, C. Liang, Y. Liu, Z. Li, G. Yang, L. Cheng, Y. Li, Z. Liu, *ACS Nano* **2013**, *7*, 6782.
[22] G. Song, Q. Wang, Y. Wang, G. Lv, C. Li, R. Zou, Z. Chen, Z. Qin, K. Huo, R. Hu, *Adv. Funct. Mater.* **2013**, *23*, 4281.
[23] M. Zheng, C. Yue, Y. Ma, P. Gong, P. Zhao, C. Zheng, Z. Sheng, P. Zhang, Z. Wang, L. Cai, *ACS Nano* **2013**, *7*, 2056.
[24] J.-G. Shiah, Y. Sun, P. Kopečková, C. Peterson, R. Straight, J. Kopeček, *J. Controlled Release* **2001**, *74*, 249.
[25] M. Y. Nahabedian, R. A. Cohen, M. F. Contino, T. M. Terem, W. H. Wright, M. W. Berns, A. G. Wile, *J. Natl. Cancer Inst.* **1988**, *80*, 739.
[26] J. Lin, S. Wang, P. Huang, Z. Wang, S. Chen, G. Niu, W. Li, J. He, D. Cui, G. Lu, *ACS Nano* **2013**, *7*, 5320.
[27] B. Jang, J.-Y. Park, C.-H. Tung, I.-H. Kim, Y. Choi, *ACS Nano* **2011**, *5*, 1086.

© 2014 WILEY-VCH Verlag GmbH & Co. KGaA, Weinheim

[28] J.-Y. Kim, W. I. Choi, M. Kim, G. Tae, *J. Controlled Release* **2013**, *171*, 113.
[29] W. S. Kuo, C. N. Chang, Y. T. Chang, M. H. Yang, Y. H. Chien, S. J. Chen, C. S. Yeh, *Angew. Chem.* **2010**, *122*, 2771.
[30] W.-S. Kuo, Y.-T. Chang, K.-C. Cho, K.-C. Chiu, C.-H. Lien, C.-S. Yeh, S.-J. Chen, *Biomaterials* **2012**, *33*, 3270.
[31] Y. Cheng, A. C. Samia, J. D. Meyers, I. Panagopoulos, B. Fei, C. Burda, *J. Am. Chem. Soc.* **2008**, *130*, 10643.
[32] B. Tian, C. Wang, S. Zhang, L. Feng, Z. Liu, *ACS Nano* **2011**, *5*, 7000.
[33] P. Huang, C. Xu, J. Lin, C. Wang, X. Wang, C. Zhang, X. Zhou, S. Guo, D. Cui, *Theranostics* **2010**, *1*, 240.
[34] C. Wang, H. Tao, L. Cheng, Z. Liu, *Biomaterials* **2011**, *32*, 6145.
[35] L. Cheng, W. He, H. Gong, C. Wang, Q. Chen, Z. Cheng, Z. Liu, *Adv. Funct. Mater.* **2013**, *23*, 5893.
[36] R. Bonnett, *Chem. Soc. Rev.* **1995**, *24*, 19.
[37] J. D. Spikes, *Ann. NY Acad. Sci.* **1975**, *244*, 496.
[38] E. Wiener, M. Brechbiel, H. Brothers, R. Magin, O. Gansow, D. Tomalia, P. Lauterbur, *Magn. Reson. Med.* **1994**, *31*, 1.
[39] L. H. Bryant, M. W. Brechbiel, C. Wu, J. W. Bulte, V. Herynek, J. A. Frank, *J. Magn. Reson. Imag.* **1999**, *9*, 348.
[40] D. L. Ladd, R. Hollister, X. Peng, D. Wei, G. Wu, D. Delecki, R. A. Snow, J. L. Toner, K. Kellar, J. Eck, *Bioconjug. Chem.* **1999**, *10*, 361.
[41] G. Kabalka, E. Buonocore, K. Hubner, T. Moss, N. Norley, L. Huang, *Radiology* **1987**, *163*, 255.
[42] R. Saito, M. T. Krauze, J. R. Bringas, C. Noble, T. R. McKnight, P. Jackson, M. F. Wendland, C. Mamot, D. C. Drummond, D. B. Kirpotin, *Exp. Neurol.* **2005**, *196*, 381.
[43] W. J. Rieter, J. S. Kim, K. M. Taylor, H. An, W. Lin, T. Tarrant, W. Lin, *Angew. Chem. Int. Ed.* **2007**, *46*, 3680.
[44] J.-L. Bridot, A.-C. Faure, S. Laurent, C. Riviere, C. Billotey, B. Hiba, M. Janier, V. Josserand, J.-L. Coll, L. Vander Elst, *J. Am. Chem. Soc.* **2007**, *129*, 5076.
[45] Z. Cheng, D. L. Thorek, A. Tsourkas, *Angew. Chem. Int. Ed.* **2010**, *49*, 346.
[46] S. Langereis, Q. G. de Lussanet, M. H. van Genderen, E. Meijer, R. G. Beets-Tan, A. W. Griffioen, J. van Engelshoven, W. H. Backes, *NMR Biomed.* **2006**, *19*, 133.
[47] P. Caravan, J. J. Ellison, T. J. McMurry, R. B. Lauffer, *Chem. Rev.* **1999**, *99*, 2293.
[48] A. E. Merbach, É. Tóth, *The chemistry of contrast agents in medical magnetic resonance imaging*, John Wiley & Sons, Ltd., Chichester **2001**.
[49] M. C. DeRosa, R. J. Crutchley, *Coord. Chem. Rev.* **2002**, *233*, 351.
[50] J. Kim, Y. Piao, T. Hyeon, *Chem. Soc. Rev.* **2009**, *38*, 372.
[51] L. Cheng, K. Yang, Y. Li, J. Chen, C. Wang, M. Shao, S. T. Lee, Z. Liu, *Angew. Chem.* **2011**, *123*, 7523.
[52] W. Cai, X. Chen, *J. Nucl. Med.* **2008**, *49*, 113S.
[53] H. Ke, J. Wang, Z. Dai, Y. Jin, E. Qu, Z. Xing, C. Guo, X. Yue, J. Liu, *Angew. Chem.* **2011**, *123*, 3073.
[54] D.-E. Lee, H. Koo, I.-C. Sun, J. H. Ryu, K. Kim, I. C. Kwon, *Chem. Soc. Rev.* **2012**, *41*, 2656.
[55] A. Louie, *Chem. Rev.* **2010**, *110*, 3146.
[56] H. Maeda, *Adv. Enzyme Regul.* **2001**, *41*, 189.
[57] P. Huang, Z. Li, J. Lin, D. Yang, G. Gao, C. Xu, L. Bao, C. Zhang, K. Wang, H. Song, *Biomaterials* **2011**, *32*, 3447.
[58] X. Liu, H. Tao, K. Yang, S. Zhang, S.-T. Lee, Z. Liu, *Biomaterials* **2011**, *32*, 144.
[59] P. Huang, J. Lin, X. Wang, Z. Wang, C. Zhang, M. He, K. Wang, F. Chen, Z. Li, G. Shen, *Adv. Mater.* **2012**, *24*, 5104.

© 2014 WILEY-VCH Verlag GmbH & Co. KGaA, Weinheim